Author/s:
Park, D;Shin, S;Sherrell, PC;Roy, B;Callaghan, KL;Caruso, F;Ellis, AV

Title:
Improving Energy Storage and Nickel Manganese Cobalt Oxide Cathode Lifetime via a Tannic Acid/Iron (III) Metal Phenolic Network Coating

Date:
2024

Citation:
Park, D., Shin, S., Sherrell, P. C., Roy, B., Callaghan, K. L., Caruso, F. & Ellis, A. V. (2024). Improving Energy Storage and Nickel Manganese Cobalt Oxide Cathode Lifetime via a Tannic Acid/Iron (III) Metal Phenolic Network Coating. Advanced Functional Materials, 35 (12), https://doi.org/10.1002/adfm.202417549.

Persistent Link:
https://hdl.handle.net/11343/354569

Improving Energy Storage and Nickel Manganese Cobalt Oxide Cathode Lifetime *via* a Tannic Acid/Iron (III) Metal Phenolic Network Coating

*Donghyuck Park, Subin Shin, Peter C. Sherrell, Binayak Roy, Kimberley L. Callaghan, Frank Caruso, Amanda V. Ellis**

D. Park, S. Shin, P. C. Sherrell, B. Roy, K. L. Callaghan, F. Caruso, A. V. Ellis

Department of Chemical Engineering, The University of Melbourne, Grattan Street, Parkville, Victoria, 3010, Australia

P. C. Sherrell

School of Science, RMIT University, Melbourne, Victoria 3000, Australia

Abstract

Surface coating lithium-ion battery cathodes is a promising strategy to improve performance and mitigate cathode degradation. The coatings studied to date focus on either electronically or ionically conducting layers, which have been introduced to enhance the redox reactions of cathode particles, or oxide-based physical protection layers limiting surface degradation. Such coatings require high-temperature, time consuming synthesis processes, along with uncertainty in the specific interactions between these coatings and lithium ions. Here we show that metal-phenolic network coated $LiNi_{0.6}Mn_{0.2}Co_{0.2}O_2$ (NMC) cathodes, produced using naturally occurring polyphenols *via* a rapid one-step assembly, improve cathode electrochemical performance. The performance improvement arises from the interaction between lithium ions and the coated layer, which enhances the lithium-ion transport to the cathode. In half-cell 1C rate cycling conditions, the modified cathode displays a 20% reduction in overpotential and a 54% decrease in interfacial resistance compared to the uncoated cathode. In a full-cell format, the modified cathode exhibits a 10% increase in capacity and a 54% increase in lifespan for constant current cycling; in addition to a 5% increase in capacity and a 25% increase in lifespan for constant current-constant voltage (CCCV) cycling. This work paves the way for improving cathode materials *via* eco-friendly lithium-ion attraction strategies.

1. Introduction

The electrification of automobiles necessitates the continued improvement of lithium-ion batteries (LIBs) to achieve a higher capacity, longer lifespan, and higher rate performance.[1] For cathode materials in LIBs, high-nickel manganese cobalt oxide (NMC), $LiNi_{1-x-y}Mn_xCo_yO_2$ ($0.6 \leq x < 1$), has emerged as a compound of choice to achieve these requirements due to its high practical capacity.[2, 3] According to the general design principle,[4] the NMC particles must be intimately assembled with carbon black (for electronic conduction) and an electrolyte (for ionic conduction) to address efficient electrochemical reactions.[5, 6] However, NMC suffers rapid degradation, which is associated with deleterious interfacial reactions between the NMC surface and the electrolyte.[7] The instability of the cathode/electrolyte interface also results in increased cell impedance,[8, 9] transition-metal dissolution,[10, 11] and intergranular cracks in the cathode secondary particles.[12]

This is the author manuscript accepted for publication and has undergone full peer review but has not been through the copyediting, typesetting, pagination and proofreading process, which may lead to differences between this version and the Version of Record. Please cite this article as doi: 10.1002/adfm.202417549.

Lithium ion (Li^+ ion) intercalation involves various pathways that consist of (1) electrolyte penetration of the porous electrode, (2) ionic transport at the cathode-electrolyte interface, (3) charge-transfer reactions, and (4) solid-state diffusion in the cathode.[13] It has been shown that the addition of a thin and conductive surface coating layer at the cathode-electrolyte interface can reduce the direct contact between NMC and the electrolyte without sacrificing performance.[14] Generally, surface coatings are made of thin layers of purpose-selected oxides (e.g., Al_2O_3, MoO_3, SiO_2),[15-17] or are determined by what the limiting factor for the charge-transfer reaction in the system is, such as ionic conductors[18, 19] and electronic conductors.[20] As surface coatings inherently shield the NMC from electrolyte contact the selection of surface coatings requires a trade-off between their ionic transfer, electronic transfer, and stability. For example, in the case of graphene coatings on a NMC, defects can be intentionally created to compensate for a decreased ionic conductivity.[5, 21] Studies have introduced extremely thin (nm scale) coatings using atomic layer deposition processes,[22] or bilayers of ion/electron conductors.[23] However, most coating layers are fabricated through the use of toxic solvents, and high energy/temperature processes, which are environmentally unsustainable.[5, 15-20, 22, 23]

Metal–phenolic networks (MPNs) are materials composed of self-assembled coordination of organic ligands with metal ions. Supramolecular metal-organic coordinated MPNs can be fabricated in a one-step assembly process (**Figure** 1a)[24] using a wide range of naturally occurring plant phenols (such as tannic acid (TA),[24] gallic acid (GA),[25] and epigallocatechin gallate (EGCG)[26]) as ligands and a variety of metal ions[27] (such as Fe^{3+}, Cu^{2+}, Al^{3+}, Zn^{2+}, Mn^{2+}, Ni^{2+}, and Co^{3+}) as coordination metals. The versatility of MPNs also allows for a broad range of functions.[28-30] For example, catechol groups (in tannic acids) can form coordination complexes with iron(III) ions (Fe^{III} ions), and the coordination complex (TA-Fe^{III}) can change in response to pH: mono-complex (pH < 2), bis-complex (3 < pH < 6), and tris-complex (7 < pH).[24] MPN formation on metal oxide surfaces is largely driven by (i) the adsorption of polyphenols on the surface of metal oxides and (ii) the polyphenol/metal ion coordination.[31, 32] As an example, galloyl-containing aromatic rings in the tannic acid can hydrogen bond with the surface oxygen groups of the NMC. Further, metal coordination bonding can occur with the surface metals of the NMC (Figure 1b and c).[33] Subsequently, the hydroxyls of the galloyl groups and the Fe^{III} ion undergo self-assembly through metal coordination, leading to TA-Fe^{III} formation.

Attempts have been made to introduce MPNs, (typically 10 nm thick),[34] with unique functionality into energy materials, with a focus on the effect on electrolyte performance. For carbon-based electrochemical capacitors, TA-Fe^{III}, which forms π-π bonding with the surface of reduced graphene oxide, increases specific capacitance by enhancing electrolyte wettability.[35] Further, uncoordinated tannic acid at the surface of single-walled carbon nanotubes has been shown to provide additional pseudocapacitance *via* a phenolic-quinone redox reaction.[36] In the case of LIBs, it has been reported that a TA-coated polypropylene separator can increase electrolyte retention and ionic conductivity by enhancing hydrophilicity.[37]

To date, there are no studies on the ionic or electronic transport within MPN coated cathode active materials for LIB applications. The interaction between MPNs and ions has remained an open question regarding their potential role within the battery system. Here, nanometer-scale coating layers of hydrophilic TA-Fe^{III} MPNs were coated onto NMC *via* a simple self-assembly approach. Cathode electrodes were then prepared from the new composite material. During electrochemical testing, in half-cell configuration, the TA-Fe^{III} coating was shown to stabilize the reactive surface of the NMC within the cathode and the unique interaction of the TA-Fe^{III} with Li^+ ions increased the electrochemical performance of the cathode.

2. Results and Discussion

A metal phenolic network of a TA-Fe^{III} complex was coated onto the surface of the active cathode material, NMC, *via* a one-step assembly process, using tannic acid and Fe^{III} ions (Figure 1a and *Experimental section*, Supporting information).[24, 38] In this work, the role of TA-Fe^{III} on the cathode active material, NMC, was studied using multiple TA-Fe^{III} deposition processes.[39] Hereon, a single TA-Fe^{III} coating on the NMC (a single layer) is denoted TA-Fe^{III}-1/NMC, two layers is denoted TA-Fe^{III}-2/NMC and four layers is denoted TA-Fe^{III}-4/NMC. From our previous literature,[24, 40] it is expected that each of the 1, 2, 4 layers corresponds to 10 nm, 20 nm and 40 nm, respectively. In this work the coatings were formed at pH = 7 and thus the TA-Fe^{III} complex formed was a bis-complex which comprises of two galloyl groups and one central Fe^{III} ion (see Figure 1b and Figure S1, Supporting information). Zeta potential results showed a change to a more negative potential with TA-Fe^{III} layers on the NMC.[24] The zeta potential of TA or TA-Fe^{III} coated NMC is independent of the inherent surface charge of NMC and reflects the surface charge of the coating layer.[24, 40] The zeta potential was shown to change from -21.7 mV for pristine NMC to approximately -37.2 mV for TA-Fe^{III}-1/NMC, TA-Fe^{III}-2/NMC, and TA-Fe^{III}-4/NMC (Figure S2, Supporting information).

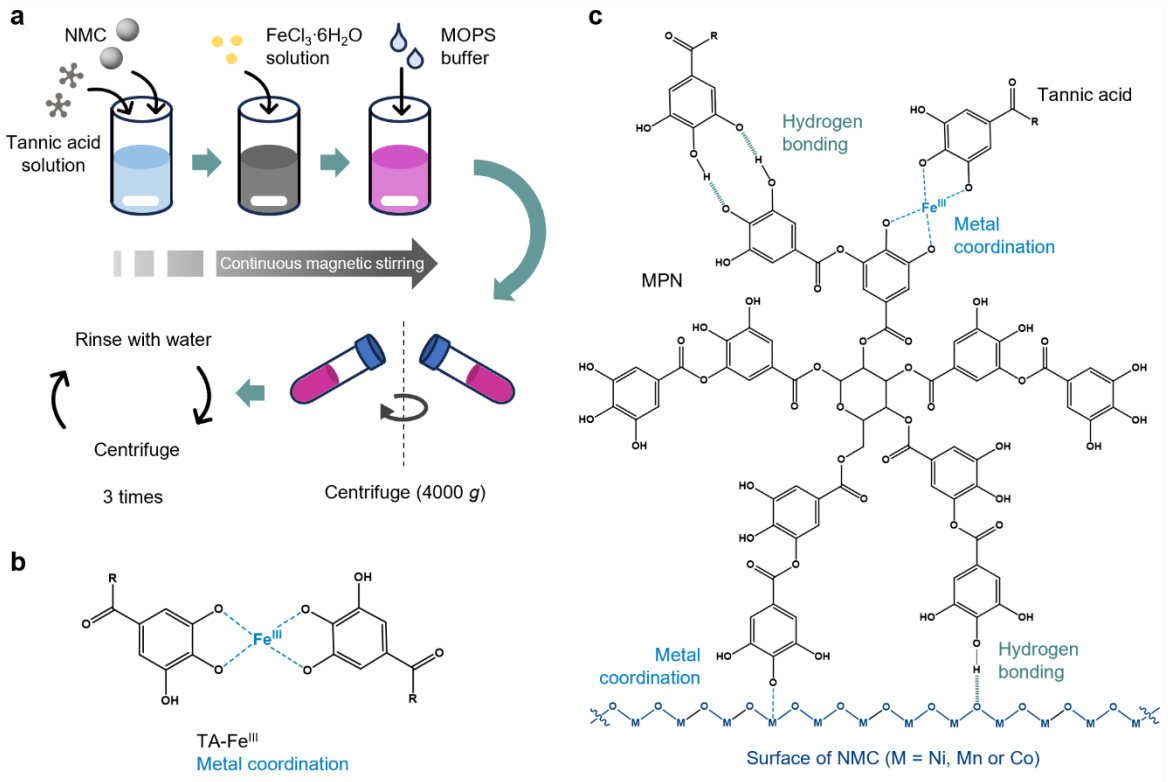

Figure 1 a) Schematic illustration of the TA-Fe^{III} coating on NMC through one-step assembly method.[24] The 3-(N-morpholino)propanesulfonic acid (MOPS) buffer was used to adjust the pH of the aqueous solution (details in *Experimental section*, Supporting information). b) Assembled polyphenol – Fe^{III} bis complex structure. R represents the rest of the tannic acid molecule. c) Proposed structure of TA-Fe^{III} coating layer on the surface of NMC. Polyphenols are absorbed on the NMC surface *via* hydrogen bonding and metal coordination. The TA-Fe^{III} is self-assembled largely *via* metal coordination bonding.

The structural and morphological properties of bulk NMC, TA-Fe^{III}-1/NMC, and TA-Fe^{III}-4/NMC were investigated using SEM and XRD (**Figure** 2a-f). For all samples, no significant difference was observed in the SEM secondary electron mode at 5k and 10k magnification, indicating that the MPN coating processes for the NMC did not disrupt NMC's original spherical structure. This is an important

consideration for active material packing in the final cathode electrode. The XRD patterns (Figure 2g-i) show highly ordered layered structures of NMC, and confirm the α-$NaFeO_2$ hexagonal-type structure (R-3m space group) of NMC, which remains unchanged after the TA/Fe^{III} coating. For all samples, the (003) facet, which defines the *c* axis of the NMC, was observed at 18.758 ± 0.009º indicating a Li^+ ion intercalated NMC lattice structure. Additionally, clear peak splitting in the (006)/(012) and (018)/(110) doublet peaks at 2 theta ~38.5º and 65º support highly ordered layered structures for all samples.[41-44] The authors note that the quantitative analysis of XRD profiles obtained *via* a Bruker D8 Advances XRD was not considered in this study due to the limited number of (low intensity) detactable peaks.

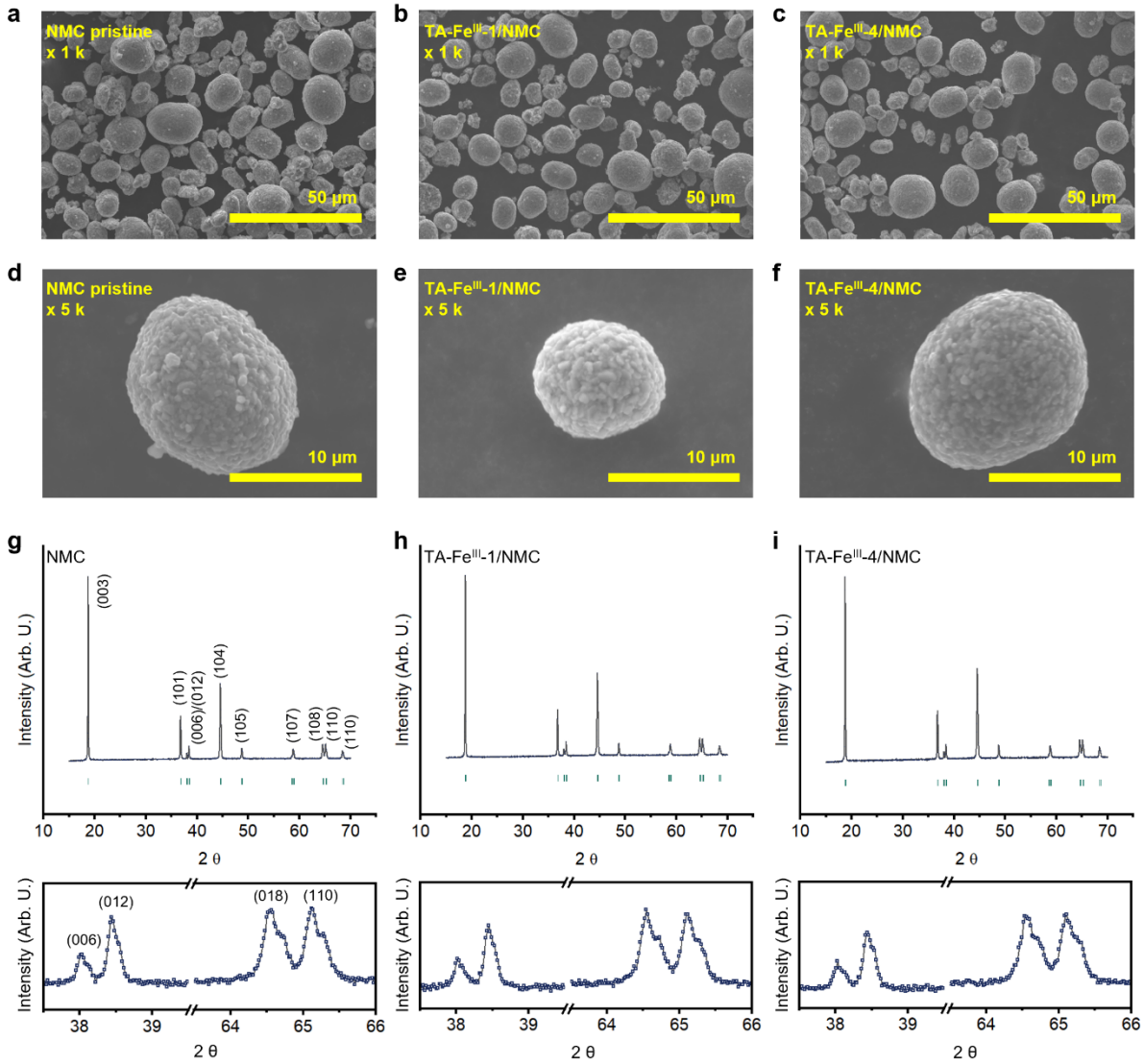

Figure 2 SEM images for a, d) NMC, b, e) TA-Fe^{III}-1/NMC and c, f) TA-Fe^{III}-4/NMC, respectively. XRD profiles for g) NMC, h) TA-Fe^{III}-1/NMC and i) TA-Fe^{III}-4/NMC. Below g-i) are the magnified XRD profiles near the (006)/(012) and (018)/(110) peak splitting.

The XPS analysis was performed to evaluate the nature of the surface on which TA-Fe^{III} was formed. A summary of curve fitting data is in Table S1, Supporting information. From the O 1s core-level spectra

(**Figure** 3a), the relative peak intensity of the lattice oxygen bond with metal (M-O, 529.06 eV) in NMC decreased as the number of TA-Fe^{III} coating layers increased. The area ratios of the (C-O, C=O)/M-O for the NMC, TA-Fe^{III}-1/NMC, TA-Fe^{III}-2/NMC, and TA-Fe^{III}-4/NMC were 1.00, 1.44, 2.21, and 4.03, respectively, indicating an increasing qualitative thickness of tannic acid on the surface (C-O and C=O moieties) with each TA-Fe^{III} coating. The Ni 2p XPS spectra (Figure 3b) show that TA-Fe^{III} converts the Ni^{2+} (854.50 eV) to Ni^{3+} (856.30 eV) on the surface of NMC. After the initial TA-Fe^{III} introduction on the NMC, the Ni^{3+}/Ni^{2+} ratio rapidly increases from 0.36 to 0.44. It is widely understood that Ni^{2+} ions in NMC cathode materials have deleterious effects on the cathode-electrolyte interface, mostly due to Li/Ni cation mixing which results in NMC phase transitions from layered to spinel or rock salt,[8] as well as transition metal dissolution.[11] TA-Fe^{III} coating appears to have oxidized the Ni^{2+} ions. This may have arisen from metal ion coordination with the deprotonated hydroxyl on the tannic acid galloyl group (Figure 1c). Yeh et al.[45] have shown that the Ni^{2+} at the surface of a Ni-rich cathode can be oxidized to Ni^{3+} by galloyl groups. In this work, the Ni^{2+} oxidation to Ni^{3+} may aid in the electrochemical performance of the active material, which will be studied later in this work.

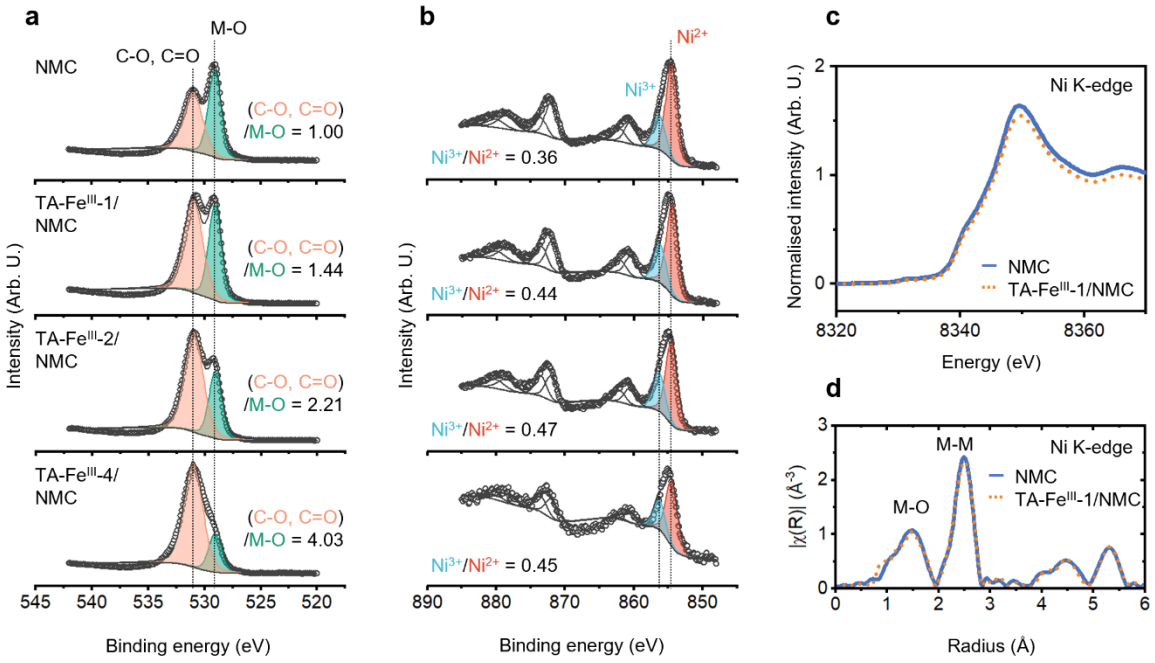

Figure 3 a) O 1s XPS spectra for NMC, TA-Fe^{III}-1/NMC, TA-Fe^{III}-2/NMC, and TA-Fe^{III}-4/NMC (Top to bottom). The (C-O, C=O)/M-O ratios were calculated from the fitted area. b) Ni 2p XPS spectra for TA-Fe^{III} coated NMC (sample order is the same as a)). c) Normalized XANES spectra of NMC and TA-Fe^{III}-1/NMC. d) EXAFS spectra of NMC and TA-Fe^{III}-1/NMC.

In order to characterize the oxidation states further and the local atomic structure of Ni, Mn, and Co within the NMC and TA-Fe^{III}-1/NMC synchrotron X-ray absorption spectroscopy (XAS) was employed. Figure 3c shows the X-ray absorption near edge structure (XANES) of NMC and TA-Fe^{III}-1/NMC at the Ni K edge, indicating an identical Ni K absorption edge (~8339.5 eV) for both the NMC and TA-Fe^{III}-1/NMC and suggesting they have comparable oxidation states. The extended X-ray absorption fine structure (EXAFS) analyses are shown in Figure 3d. The M-O peaks at ~1.5 Å originate from the Ni-O interaction of the first coordination shell while the M-M peaks at ~2.5 Å are from the Ni-Ni interaction.[46] The EXAFS analysis also affirms that NMC and TA-Fe^{III}-1/NMC demonstrate similar M-O (Ni-O at ~1.5 Å) and M-M (Ni-Ni at ~2.5 Å) interaction peaks. The minor difference between NMC and TA-Fe^{III}-1/NMC at R ~1 Å is most likely due to an artefact of incomplete background removal.[47] Furthermore, no

significant differences between NMC and TA-Fe^{III}-1/NMC were observed in the XANES and EXAFS analyses for Mn and Co (Figure S3, Supporting information). The results of the oxidation state and local atomic structure are all in agreement with previously reported results for Ni-rich cathodes.[46, 48]

For investigation of the Fe^{III} ions in TA/Fe^{III}, the XPS Fe 2p spectrum of TA/Fe^{III}-4/NMC is shown in Figure S4a, Supporting information. The weak signal for Fe 2p, originating from a relatively low Fe content, was filtered using Fast Fourier Transform (FFT, cutoff 0.25 Hz). The Fe^{3+} $2p_{3/2}$ (711.3 eV) shows the predominance of the 3+ oxidation state of Fe in TA/Fe^{III}, but Fe $2p_{1/2}$ suggests the potential presence of Fe^{2+}.[49] For the presence of Fe in TA/Fe^{III}, XANES Fe K edge for TA/Fe^{III}-1/NMC also exhibited a rising main absorption edge and a main peak for Fe (Figure S4b, Supporting information). The characteristically lower Fe signal intensity compared to Ni, Mn, and Co signals indicates that a nanometer-scale TA-Fe^{III} layer has formed on the NMC surface, implying that Fe^{3+} is the metal ion source for the metal phenolic networks.

Cyclic voltammetry (CV) measurements were conducted to investigate the effect of the TA-Fe^{III} layers on the electrochemical properties of NMC. The CV was carried out in the range of 3.0 V to 4.3 V vs. Li^+/Li at various scan rates from 0.1 to 1.0 mV s^{-1} in half-cell format with Li metal as a counter electrode and 1 M $LiPF_6$ EC/EMC (30/70 wt/wt) + 2% VC electrolyte (see *Experimental section*, Supporting information). For the NMC, one redox peak was observed during charging (anodic) and discharging (cathodic), shown in **Figure** 4a. At 0.1 mV s^{-1} scan rate, NMC showed an anodic peak at 3.81 V and cathodic peak at 3.68 V vs. Li^+/Li. As the scan rate was increased, the peak potential separation between anodic and cathodic peaks broadened by shifting the current peaks to either end of the voltage window (4.04 V for anodic and 3.53 V for cathodic at 1.0 mV s^{-1} scan rate). This broadened peak potential separation means increased polarization originating from a limited charge-transfer reaction on the NMC's quasi-reversible electrochemical reaction.

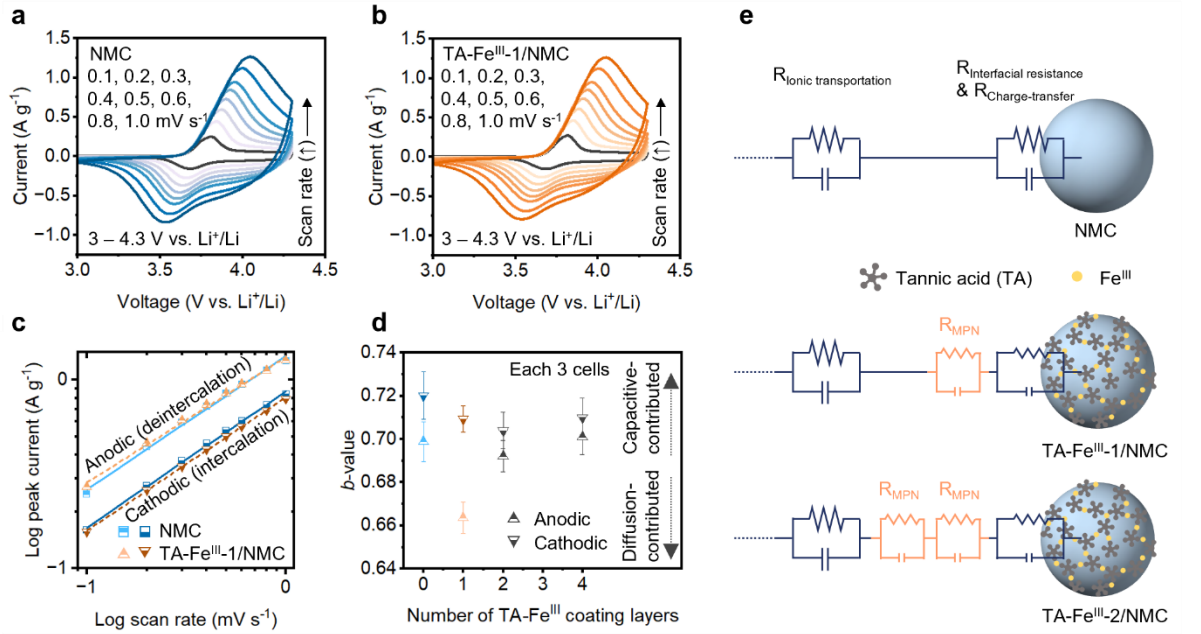

Figure 4 Charge storage kinetic analysis. The cyclic voltammetry (CV) curves on 0.1 – 1.0 mV s^{-1} scan rates in the range of 3.0 – 4.3 V vs. Li^+/Li for a) NMC and b) TA-Fe^{III}-1/NMC. c) The relationship between peak current and scan rate during charging (anodic) and discharging (cathodic). d) Calculated *b*-value of NMC, TA-Fe^{III}-1/NMC, TA-Fe^{III}-2/NMC and TA-Fe^{III}-4/NMC. The error bar represents the standard deviation. e) Schematics of equivalent electrical circuits on NMC, TA-Fe^{III}-1/NMC, and TA-Fe^{III}-2/NMC.

As it is difficult to visually compare NMC and TA-Fe^{III} -1/NMC based on raw CV curves alone (Figure 4a and b), electrochemical energy storage mechanisms were used to distinguish between a surface capacitive contribution and an ionic diffusion contribution.[50, 51] Thus, following a power law (Equation 1), the dependence of the CV measured peak current with scan rate variation can provide information on the mechanism behind the electrochemical process.[52-54]

$$i = av^b \qquad \text{Equation 1}$$

where i is the peak current density [A g^{-1}], v is a scan rate [mV s^{-1}], and a and b are adjustable parameters. When the b value is close to 0.5, it indicates that the electrochemical reaction is ionic diffusion dominated. On the other hand, when the b value is close to 1.0, it indicates capacitive behavior. As an example, Figure 4c shows the power law relationship between peak current and scan rate for NMC and TA-Fe^{III}-1/NMC. The b value is represented by the slope for both the anodic and cathodic plots. To understand the role of TA-Fe^{III} for the charge storage mechanism, b values for NMC, TA-Fe^{III}-1/NMC, TA-Fe^{III}-2/NMC, and TA-Fe^{III}-4/NMC were plotted versus the coating layers in Figure 4d. The b values of NMC were 0.70 ± 0.01 for the anodic reaction and 0.72 ± 0.01 for the cathodic reaction. Interestingly, TA-Fe^{III}-1/NMC showed lower b values, 0.66 ± 0.01 and 0.71 ± 0.01 for anodic and cathodic, respectively, indicating higher ionic (de)intercalation contributions compared to NMC alone. As the TA-Fe^{III} coating layers increased, the b values approached 1, showing an increasing surface capacitive contribution.

For the ionic (de)intercalation reaction, the Li^+ ions reach the surface of the NMC *via* electrolyte penetration of the porous electrode structure ($R_{Ionic\ transportation}$) and undergo charge-transfer reactions at the interface ($R_{Charge\text{-}transfer}$ + $R_{Interfacial\ resistance}$). For TA-$Fe^{III}$-1/NMC, the TA-$Fe^{III}$ coating layer can attract Li^+ ions due to their inherent negative charge (see Figure S2 zeta potential analysis and Figure S5 UV-vis analysis, Supporting information) thus increasing the ability of Li^+ ions to reach the active material NMC for (de)intercalation reaction. The increased Li^+ ion accessibility can reduce interfacial resistance and charge-transfer resistance, resulting in enhanced ionic (de)intercalation reactions. For the TA-Fe^{III}-2/NMC and TA-Fe^{III}-4/NMC, there is expected to be the same density of charge at the cathode-electrolyte interface as TA-Fe^{III}-1/NMC (Figure S2, Supporting information). However, the longer ionic path is greater due to the increasing thickness after each coating,[39] meaning that the Li^+ ions have to overcome strong electrostatic interactions (R_{MPN}). This results in a slow-moving ionic transport of Li^+ ions (great b value) and consequently an increased surface capacitive contribution (Figure 4e).

To further investigate the effect of the TA-Fe^{III} layers on the Li^+ ion (de)intercalation reaction of NMC, the galvanostatic intermittent titration technique (GITT) was carried out in the potential range of 3.0 – 4.3 V vs. Li^+/Li using a series for 0.25 h at C/10 rate current pulse each, followed by a 5 h rest period (**Figure** 5a). During LIB battery cycling, the voltage contributes not only to the thermodynamic equilibrium state of the NMC, depending on the amount of Li^+ ions inside, but also the overpotential such as ionic transportation and charge-transfer reactions.[55] For GITT, at charging (Figure 5b) when a positive current pulse is applied to an electrode with a homogeneous mobile ion concentration, a sudden voltage step occurs, and the voltage continues to increase. When the applied current is relaxed during a subsequent rest period, the voltage reaches thermodynamic equilibrium at the open-circuit voltage (OCV).[56] When discharging, the voltage response is reversed due to the negative current pulses (Figure 5c). The overpotential can be obtained as the difference between the increased voltage and the OCV.

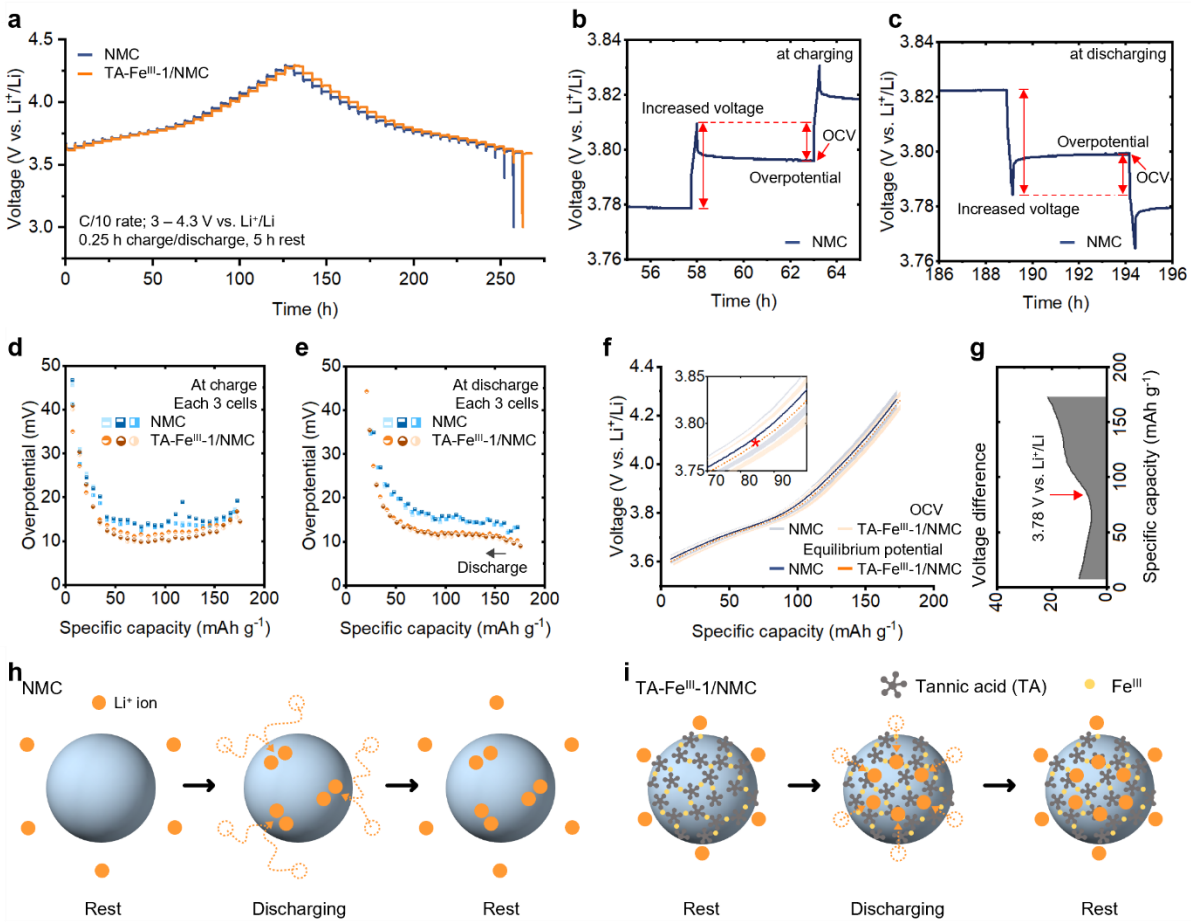

Figure 5 a) Galvanostatic intermittent titration (GITT) measurement in the range of 3 – 4.3 V vs. Li^+/Li using C/10 rate current pulse for 0.25 h and 5 h relaxation period (1C rate = 276.5 mAh g^{-1}). The voltage response of NMC in the range of 3.76 – 3.80 V vs. Li^+/Li during b) charging and c) discharging. The observed overpotentials during d) charging and e) discharging. f) Open circuit voltages (OCV, error bands represent standard deviation) during charging (top) and discharging (bottom). Equilibrium potential is estimated by averaged OCV at the same SOC. 3.78 V vs. Li^+/Li is marked with an asterisk. g) Equilibrium potential difference between NMC and TA-Fe^{III}-1/NMC. Schematics of Li^+ ion diffusion in h) NMC and i) TA-Fe^{III}-1/NMC.

The overpotentials were investigated using three identical electrodes for each of the NMC and TA-Fe^{III}-1/NMC samples during charging and discharging (Figure 5d and e). When the NMC (theoretical capacity = 276.5 mAh g^{-1}) was charged from 55.3 mAh g^{-1} to 165.9 mAh g^{-1} (corresponding to a 0.8 and 0.4 Li^+ ion fraction, respectively), the average overpotential was observed to be 14.3 mV for charge and 15.3 mV for discharge (Figure S6a and b, Supporting information). In the case of the TA-Fe^{III}-1/NMC, results showed 11.4 mV for charge and 11.7 mV for discharge. These reduced overpotentials of the TA-Fe^{III}-1/NMC are important and indicative of a more effective ionic (de)intercalation reaction. Further, it supports the claim that an increased charge transfer reaction is associated with increased access of Li^+ ions into and out of the one-layer TA-Fe^{III}. For TA-Fe^{III}-2/NMC and TA-Fe^{III}-4/NMC, the overpotentials were 14.0 mV and 16.0 mV for charging and 14.0 mV and 15.2 mV for discharging, respectively (Figure S6c-e, Supporting information). Clearly, as the layers increased the overpotentials increased, increasing the surface capacitive contribution.

To investigate the structural phase transitions occurring during electrochemical testing, OCV analysis derived from GITT was used. The NMC particles exhibit structural phase transitions depending on the amount of Li^+ ions in the crystal lattice. Poor structural phase transitions can lead to heterogeneous volume changes in the NMC, resulting in local strain concentration and thus structural instability.[57] In the GITT charge-discharge profile, a plateau was observed in 3.75 – 3.80 V vs. Li^+/Li for both NMC and TA-Fe^{III}-1/NMC. At the plateau voltage, the greatest capacity is observed and a H1 ↔ H2 structural phase transition (H1: R-3m, a = 2.86 Å and c = 14.227 Å; H2: R-m, a = 2.81 Å and c = 14.37 Å) commences.[58] To evaluate the electrochemical efficiency of this structural phase transition, equilibrium potentials were investigated, see Figure 5f. The OCVs of NMC and TA-Fe^{III}-1/NMC are presented as error bars, and the equilibrium potentials are determined by averaging OCVs at the same state-of-charge (SOC). Note, the OCV does not reflect the actual thermodynamic equilibrium state of the NMC and can contain voltage hysteresis (i.e., electrochemical inefficiencies).[59, 60]

The equilibrium potential difference between NMC and TA-Fe^{III}-1/NMC is displayed in Figure 5g. Here, NMC shows a slightly higher equilibrium potential compared to TA-Fe^{III}-1/NMC at the same SOC up to ~85 mAh g^{-1} (where x = ~0.7 in $Li_xNi_{0.6}Mn_{0.2}Co_{0.2}O_2$). This causes hindered Li^+ ion transport onto the surface of the NMC resulting in the generation of an ionic concentration gradient at the cathode-electrolyte interface. This is supported by a lower overpotential for the TA-Fe^{III}-1/NMC originating from polarization from the ionic concentration gradient.

After the structural phase transition began (above ~3.78 V vs. Li^+/Li), the equilibrium potential difference rapidly increased. Compared to the TA-Fe^{III}-1/NMC, the uneven ability of Li^+ ions to reach the NMC surface resulted in an inhomogeneous local structural phase transition leading to voltage hysteresis. It is noted that inhomogeneous structural phase transition can lead to heterogeneous volume changes on the NMC, resulting in local strain concentration and thus structural instability.[57] Figure 5h shows a schematic of the inhomogeneous Li^+ ion diffusion on the NMC. In contrast, Figure 5i schematically demonstrates that the increased ability of Li^+ ions to reach the active material NMC on the TA-Fe^{III}-1/NMC acts to mitigate the inhomogeneous local H1 ↔ H2 transition resulting in a more efficient electrochemical reaction. The GITT results suggest that TA-Fe^{III} not only reduce overpotential by increasing the ability of Li^+ ions to reach the NMC for the (de)intercalation reaction but also lead the efficient structural phase transition to the NMC.

In order to gain insights into the cause of the improved Li^+ ion accessibility by the TA-Fe^{III} coating, EIS was employed. EIS provides a series of complex resistance (or impedance) components that can occur at the cathode-electrolyte interphase, during the charge-transfer reaction, and from solid-state diffusion.[61] **Figure** 6a shows the EIS spectra of NMC (blue), TA-Fe^{III}-1/NMC (orange), TA-Fe^{III}-2/NMC (pale green) and TA-Fe^{III}-4/NMC (dark green) at 3.80 V vs. Li^+/Li. These EIS spectra comprise of four regions:[6] (i) an intercept at very high frequency (>10 kHz), describing combinations of ohmic resistances (electrical resistance of electrolyte, current collector and separator) and an electrical double layer capacitance (EDLC); (ii) a semicircle at high frequency (nearby frequencies between 10 kHz and 100 Hz), representing interfacial resistance (e.g., cathode-electrolyte interphase resistance); (iii) a relatively small semicircle at intermediate frequencies (~100 Hz to ~1 Hz) associated with the charge-transfer reaction; and (iv) a Warburg tail at low frequency (<1 Hz) from solid-state diffusion. Overall, it was observed that the impedance was notably reduced for TA-Fe^{III}-1/NMC compared to NMC, however with further TA-Fe^{III} layers the impedance increased (overlayed Nyquist plots for all samples are shown in Figure S7a, Supporting information).

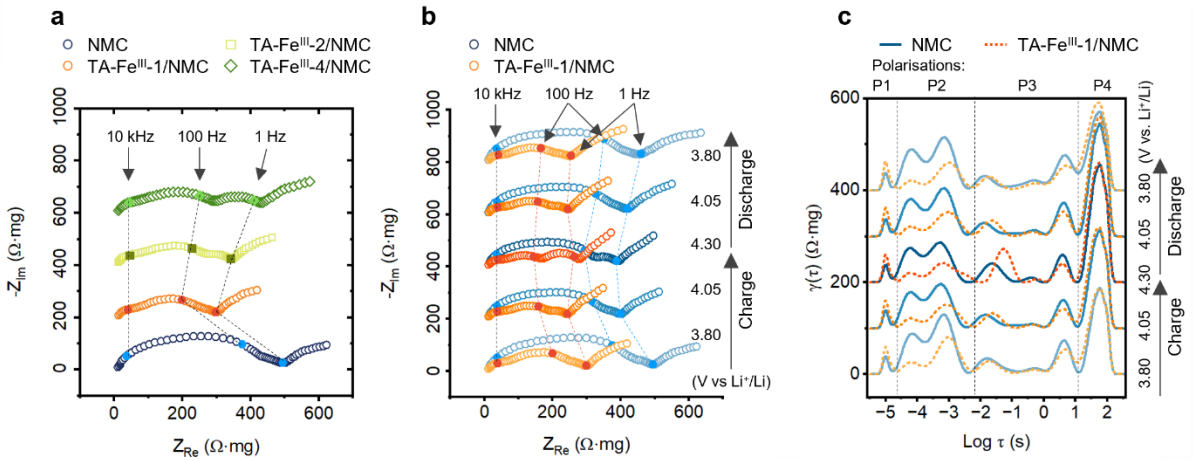

Figure 6 Electrochemical impedance spectroscopy measurement. a) Nyquist plots of NMC (blue), TA-Fe^{III}-1/NMC (orange), TA-Fe^{III}-2/NMC (pale green) and TA-Fe^{III}-4/NMC (dark green) at 3.80 V vs. Li$^+$/Li. b) Nyquist plots of NMC and TA-Fe^{III}-1/NMC at 3.80 V, 4.05 V and 4.30 V vs. Li$^+$/Li during charge and discharge. c) Distribution of relaxation times (DRT) of NMC and TA-Fe^{III}-1/NMC corresponding to b).

The intercept values of real impedance (Z_{Re}) showed negligible differences in all samples, indicating similar ohmic resistances and EDLC impedances (Figure 6a). However, TA-Fe^{III}-1/NMC showed a significantly lower interfacial resistance compared to NMC, represented by the first semi-circle at high frequency. This is expected and confirms CV, GITT results as it shows that the TA-Fe^{III} coating layer is able to coordinate Li$^+$ ions (through the galloyl groups on the TA ligand) at the cathode-electrolyte interface. This interfacial resistance increases with TA-Fe^{III}-2/NMC and TA-Fe^{III}-4/NMC because the thicker the negatively charged TA-Fe^{III} layer, the longer the diffusion path the Li$^+$ ions need to overcome in order to reach the NMC surface for electrochemical reaction. Likewise, the charge-transfer reaction follows a similar trend to the interfacial resistance, although semi-circles were ambiguously observed. Further, the Warburg tails, from solid-state diffusion, are the same for all samples. For NMC and TA-Fe^{III}-1/NMC, the phenomenon of reduced electrochemical impedance of NMC by TA-Fe^{III} was observed in the range across charge and discharge (Figure 6b). However, in the case of semi-circles near 100 – 1 Hz at 4.30 V vs. Li$^+$/Li for the TA-Fe^{III}-1/NMC were larger than the NMC indicating that the TA-Fe^{III}-1/NMC had a higher charge-transfer impedance than the NMC. This phenomenon may be caused by various factors and will be discussed later.

To understand the kinetic mechanisms involved during electrochemical testing of the TA-Fe^{III} coated NMC, the distribution of relaxation times (DRT) technique was used. The DRT technique is useful for characterizing electrochemical kinetic processes that are ambiguously represented by Nyquist plots due to their close relaxation times.[62] With an approach that the external electrical stimulation can induce the relaxation processes for the electrochemical processes, Li$^+$ ion (de)intercalation for NMC cathodes can be interpreted as a series of parallel RC elements circuit (Figure 4e).[63]

Figure 6c shows the DRT plots for NMC and TA-Fe^{III}-1/NMC during charge and discharge. The four polarization regimes can be distinguished by their relaxation time: EDLC (P1), Interfacial reaction (P2), charge-transfer reaction (P3), and solid-state diffusion (P4). The fitting curves and residuals for the DRT analysis are presented in Figure S8, Supporting information. TA-Fe^{III}-1/NMC showed a higher EDLC compared to NMC (log τ ~ -5.0) (Figure 6c, P1), a result of secondary interactions within the TA-Fe^{III} such as π-cation and electrostatic interactions with monovalent ions which can enhance EDLC formation.[64] It is important to note that the EDLC is a faster charge storage mechanism than a pseudocapacitive mechanism. The capacitive contribution observed in the CV (Figure 4a) where the

peaks can be found is mainly caused by a pseudocapacitive contribution rather than an EDLC.[65] In the case of interfacial resistance at charge 3.80 V vs. Li^+/Li, NMC and TA-Fe^{III}-1/NMC show 88 Ω·mg, 26 Ω·mg at log τ ~ -4.2 and 130 Ω·mg, 80 Ω·mg at log τ ~ -3.1, respectively. It is still currently difficult to determine the exact kinetic process for each peak due to possible complex behavior such as ionic conduction at the bulk and at the contact interface, however, the concept that P2 refers to interfacial resistance is supported by the empirically investigated relaxation time of the interfacial resistance.[66] TA-Fe^{III}-1/NMC clearly shows a reduced interfacial resistance resulting from enhanced the ability of Li^+ ions to reach the NMC (Figure 6c, P2).

For the charge-transfer reaction (Figure 6c, P3), the most responsive polarization of NMC (log τ ~ -1.8) increased during charging (34.4 Ω·mg to 41.2 Ω·mg) and then returned to a similar level during discharging (31.3 Ω·mg at discharge 3.80 V vs. Li^+/Li). TA-Fe^{III}-1/NMC showed 28.9 Ω·mg (log τ ~ -1.72), which was lower and slower than for the NMC at 3.80 V vs. Li^+/Li. This suggests that although TA-Fe^{III} increases Li^+ ion accessibility for the ionic intercalation reaction on NMC, the electrostatic interaction between TA-Fe^{III} and the Li^+ ions may act to hinder ionic transportation. This is also confirmed by the incremental increase in the charge-transfer resistances for TA-Fe^{III}-2/NMC (43 Ω·mg at log τ ~ -1.61) and TA-Fe^{III}-4/NMC (73.1 Ω·mg at log τ ~ -1.33) (see Figure S7b, Supporting information).

For the TA-Fe^{III} coated samples, the sharp increase in charge-transfer resistance at 4.30 V vs. Li^+/Li remains unclear but there are several possible scenarios. Firstly, stabilized surface reactive oxygen in NMC through chemical interaction with TA-Fe^{III} can suppress unstable oxygen redox reactions generally occurring at high voltage (i.e., high state-of-charge). While oxygen redox offers additional capacity beyond transition metal redox reactions, it has been understood as an unfavorable reaction that leads to structural degradation due to irreversible oxygen gas release.[57, 67] Another possible scenario is the competitive bidirectional movement of Li^+ ions at the TA-Fe^{III} ··· NMC interface due to the ionic concentration gradient. The deficiency of Li^+ ions in the deintercalated NMC local lattice can be polarized towards the TA-Fe^{III}, where Li^+ ions are grouped. The direction of polarization is opposing the direction of Li^+ ions during charging, might hinder additional deintercalation from the NMC lattice (i.e., ion regulation)[68]. In terms of the DRT results, it should be considered that the increment of charge-transfer resistance is reversible and is mitigated during subsequent intercalation (Figure 6c) and is also seen in TA-Fe^{III}-2/NMC and TA-Fe^{III}-4/NMC (Figure S7c and d, Supporting information). The charge-transfer resistances at log τ ~ 0.62 were observed to be overall similar or somewhat lower for TA-Fe^{III}-1/NMC compared to NMC during charge and discharge, with the same level of P4 associated with solid-state diffusion.

The NMC and TA-Fe^{III} coated NMC cathodes were evaluated *via* galvanostatic charge-discharge technique in the range of 3.0 – 4.3 V vs. Li^+/Li for battery performance. For the rate performance of the cathode half-cells (**Figure** 7a), all samples showed similar capacity of ~175 mAh g^{-1} at C/20 rate. The practical capacity of NMC (175 mAh g^{-1}) aligns with values reported in earlier studies.[69, 70] As the C-rate was increased to 3C rate, the difference in rate performance of the cathode half-cells was observed to be more significant. Compared to NMC, TA-Fe^{III}-1/NMC showed a 2.2%, 3.3%, 3.9%, and 4.4% improvement in discharge capacity at C/2, 1C, 2C, and 3C rate, respectively (Table 1, Figure S9a and b, Supporting information). It is well understood that compared to a low C-rate, a high C-rate promotes higher ionic mobility across the cathode interface, which consequently results in a higher ionic concentration gradient at the cathode-electrolyte interface.[71] This gradient gives rise to local polarization, which increases the cell voltage and hinders the homogeneous Li^+ ion (de)intercalation. Additionally, the local polarization triggers unstable oxygen redox reactions at the surface of the NMC, [71] as well as electrolyte decomposition and lithium dendrite formation.[72, 73] These side reactions, such as oxygen redox and electrodeposition, are inherently irreversible during charging and discharging, which negatively affects cycling performance efficiency. Thus, having 1 layer of the TA-Fe^{III}, which

absorbs Li^+ ions in response to ionic concentration, alleviates the polarization and makes the de(intercalation) reaction more homogeneous, resulting in an improved rate performance.

In contrast, TA-Fe^{III}-4/NMC exhibited 9.4%, 14.1%, 16.5%, and 18.2% capacity reduction at C/2, 1C, 2C and 3C rate compared to NMC, with capacity decreasing with increasing C-rate (Figure S9d, Supporting information). This is because the increased charge-transfer resistance from the longer diffusion pathway in the multi-layered TA-Fe^{III} has a negative impact on the overall cathode performance relative to the improved ability of Li^+ ions to reach the NMC observed in the TA-Fe^{III}-1/NMC.

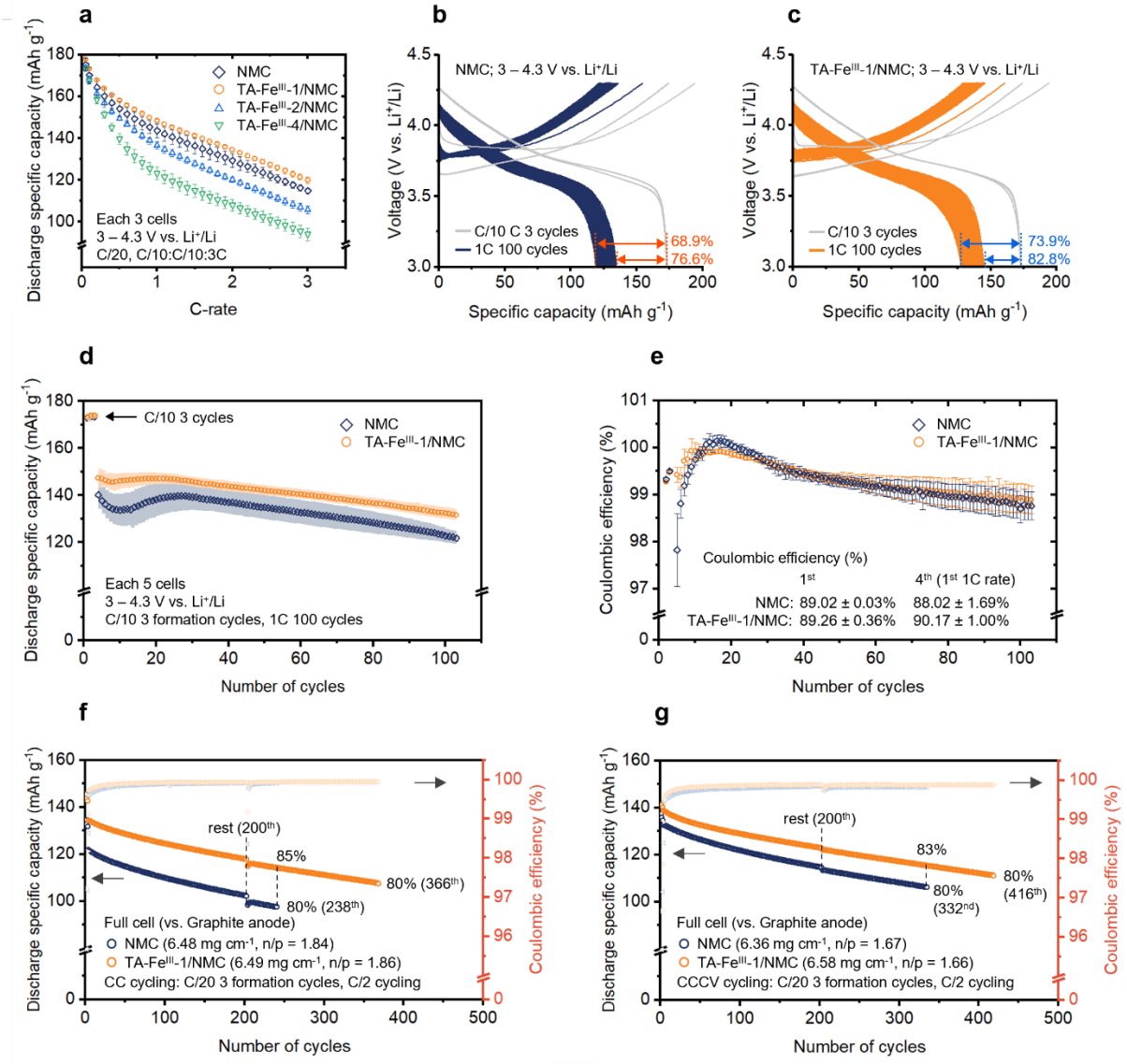

Figure 7 Battery test results. The C-rate is calculated based on the theoretical capacity of 276.5 mAh g^{-1}. a) Rate performance of NMC, TA-Fe^{III}-1/NMC, TA-Fe^{III}-2/NMC and TA-Fe^{III}-4/NMC on C/20 to 3C rate. The cathode half cells were subjected to C/10 rate 3 cycles formation process before the rate performance test. Error bars represent standard deviations. GCD curves for cathode half-cells at C/10 rate 3 cycles and subsequent 1C rate 100 cycles: b) NMC and c) TA-Fe^{III}-1/NMC. d) Discharge specific capacity of NMC and TA-Fe^{III}-1/NMC for 1C rate 100 cycles. The error bands represent standard deviations. e) Coulombic efficiency for 1C rate 100 cycles. The coulombic efficiencies of the 1st and 4th cycles, which are not shown on the Y-axis scale, are labelled. Discharge specific capacity of NMC and

TA-Fe^{III}-1/NMC in full-cell format using f) constant current (CC) charge – CC discharge cycling and g) constant current constant voltage (CCCV) charge – CC discharge cycling.

The specific capacity is rate-dependent, and the time constant associated with charge-discharge cycling can be characterized (see details in Figure S10, Supporting information).[74] The TA-Fe^{III} is anticipated to exert a dual effect on the (de)intercalation reaction on NMC by enhancing the ability of ions to reach the active material while also creating an electrostatic barrier that the ion must navigate. The comparison of time constants provides evidence for how much the electrostatic barrier delays the (de)intercalation reaction. The time constants for NMC, TA-Fe^{III}-1/NMC, TA-Fe^{III}-2/NMC, and TA-Fe^{III}-4/NMC were estimated to be 79.60 ± 2.09, 77.08 ± 3.57, 93.28 ± 2.24, and 134.42 ± 9.65 s, respectively. The addition of the TA-Fe^{III} to NMC results in a near identical measured surface charge regardless of layer number (~-37 mV zeta potential for 1-layer, 2-layer, and 4-layer TA-Fe^{III} coated NMC, increased from -22 mV for pristine NMC, Figure S4, Supporting information). This near identical surface charge indicates the solution-cathode interface is dominated by the TA-Fe^{III} structure, suggesting that the observed decrease in electrochemical performance at TA-Fe^{III}-2/NMC and TA-Fe^{III}-4/NMC arises due to the thickness of the layers limiting the Li^+ (de)intercalation process. This is supported by the linear increase in time constant with TA-Fe^{III} layer number for the rate-dependent performance of the cathode (from 77.08 ± 3.57s to 134.42 ± 9.65 s for 1 layer and 4 layers respectively, Figure S10b, Supporting information) highlighting a higher layer number slows the kinetics of the (de)intercalation reaction despite the equivalent surface charge.

The GCD curves for NMC and TA-Fe^{III}-1/NMC half-cells on 1C rate 100 cycles are shown in Figure 7b and c. The half-cells were subjected to a formation process at C/10 rate for 3 cycles. During the formation process, NMC and TA-Fe^{III}-1/NMC depicted similar discharge specific capacity of ~173 mAh g^{-1} and initial coulombic efficiency (CE) of ~89%. Compared to C/10 rate initial 3 cycles (i.e., formation cycles), the 1C rate first cycle showed 76.6% capacity retention for NMC and 82.8% for TA-Fe^{III}-1/NMC. At the 1C rate 100^{th} cycle, NMC and TA-Fe^{III}-1/NMC retained 68.9, 73.9%, respectively. For each of the 5 half-cells, the average discharge capacity and its standard deviation are given in Figure 7d. The NMC only allowed capacities of 140.1 ± 5.9, 134.2 ± 5.1 and 121.8 ± 2.6 mAh g^{-1} for the 1^{st}, 50^{th} and 100^{th} 1C rate cycling, respectively. However, TA-Fe^{III} -1/NMC showed 147.26 ± 4.05, 141.56 ± 2.12 and 131.60 ± 2.57 mAh g^{-1}, respectively. Compared to initial capacity (173 mAh g^{-1} at C/10 rate), TA-Fe^{III}-1/NMC maintained a 76% discharge capacity after 1C rate 100 cycles, which is higher than NMC (70%).

Interestingly, NMC showed unstable performance for the first 30 cycles compared to TA-Fe^{III}-1/NMC and then gradually stabilized. This is probably due to the reconstruction of the electrode-electrolyte interphase by the locally concentrated Li^+ ions at the interface as seen in literature.[75, 76] This phenomenon can also be confirmed by the CE shown in Figure 7e. For the initial CE, both NMC and TA-Fe^{III}-1/NMC exhibit similar CE's of 89.02 ± 0.36% and 89.26 ± 0.03 %, respectively. However, the CE of NMC for the first 1C rate cycle only showed 88.02 ± 1.69 %, in sharp contrast, TA-Fe^{III}-1/NMC delivered 90.17 ± 1.00 %. During 30 cycles, TA-Fe^{III}-1/NMC showed stable cycling performance compared to NMC, with the CE not exceeding 100%. In the case of NMC, CE is above 100% on cycles 13^{th} – 21^{st}, indicating higher discharge capacity than charge. This suggests that the interphase reconstruction (e.g., electrodeposition or stripping) is involved in the unstable charge storage mechanism at the 1C rate.

Finally, NMC and TA-Fe^{III}-1/NMC were prepared in a full-cell format using graphite anodes, and the cycling performances at C/2 rate were investigated (Figure 7f and g). The n/p ratio of the full-cells was designed to be higher than 1.5 for evaluating cathode-limited cycling performance[77] (with $Q/M_{cathode}$ = 150 mAh g^{-1} and Q/M_{anode} = 350 mAh g^{-1}). For the constant current (CC) cycling (Figure 7f), TA-Fe^{III}-1/NMC showed a 10% improved discharge capacity over NMC in the first C/2 rate cycle, reaching

134.36 mAh g^{-1}. This is attributed to the enhanced ability of Li^+ ions to reach the active material NMC for (de)intercalation reaction by TA-Fe^{III}, which is the same enhancement mechanism that improved the rate performance of the TA-Fe^{III}-1/NMC. By the 238th C/2 rate cycle, the NMC retention rate reached 80%, while the retention rate of TA-Fe^{III}-1/NMC was greatly improved at 85%. TA-Fe^{III}-1/NMC then delivered 80% of its first C/2 rate cycle capacity by the 366th cycle. For the constant current constant voltage (CCCV) charge – CC discharge cycling, NMC exhibited 80% retention of its initial C/2 rate capacity by the 332nd cycle, whereas TA-Fe^{III}-1/NMC reached this level by the 416th cycle number. CCCV charge is a charging method where the voltage is held constant at 4.3 V after CC charge (i.e., galvanostatic charge), allowing some portion of NMC overpotential to relax. Despite the overpotential compensation by constant voltage, TA-Fe^{III}-1/NMC demonstrated a 4.7% improved capacity, and a 25.3% longer lifespan compared to NMC. This is likely because the TA-FeIII coating layer not only reduces overpotential but also provides advantages for ionic transport and the structural phase transition of the cathode. A comparison with previously reported coating materials, synthesis processes and cycling performances is provided in Table S2, Supporting information.

Table 1. Averaged discharge capacity for cathode half-cells.

Sample	Rate performance (mAh g^{-1})				Cycling performance (mAh g^{-1})
	C/5	C/2	1C	2C	
NMC	164.3 ± 3.9	154.2 ± 3.6	143.6 ± 3.3	129.3 ± 3.3	121.7 ± 2.6 at 1C 100 cycles
TA-Fe^{III}-1/NMC	167.8 ± 0.4	158.0 ± 0.9	148.3 ± 0.9	134.4 ± 0.9	131.6 ± 2.6 at 1C 100 cycles
TA-Fe^{III}-2/NMC	161.4 ± 2.3	149.5 ± 0.7	136.7 ± 1.7	120.2 ± 1.4	
TA-Fe^{III}-4/NMC	158.5 ± 1.9	139.8 ± 2.5	123.3 ± 3.0	107.9 ± 2.8	

3. Conclusions

In summary, this work demonstrated the efficacy of a one-step self-assembled tannic acid-iron(III) metal-phenolic network coating on the surface of a cathode active material, NMC, for LIBs. The underlying mechanism for improved battery performance was elucidated, while the coating still maintained the inherent properties of the bulk NMC such as morphology, crystal lattice structure, electronic state, and resistance to solid-state diffusion. It was shown that the absorption of polyphenols oxidized the Ni^{2+} to Ni^{3+} at the surface of the NMC, which caused Li/Ni cation mixing. TA-Fe^{III}-1/NMC provided the greatest improvement in the ability of Li^+ ions to reach the NMC surface with reduced overpotentials of 20% on charge and 24% on discharge compared to NMC in the range of 0.8 – 0.4 Li^+ ion fraction in NMC. In addition, TA-Fe^{III}-1/NMC improved the homogeneity of the (de)intercalation reaction on the NMC surface, reducing the equilibrium potential by up to 21.5 mV in terms of thermodynamic structure-related open circuit voltage. From a kinetic perspective, the TA-Fe^{III}-1/NMC was shown to reduce the interfacial resistance by an average of 54% for the Li^+ ion (de)intercalation reaction. This resulted in a 4.44% capacity increase in the rate performance and a 6% improvement in retention at 1C rate after 100 cycles. An improvement in coulombic efficiency was also observed at high rates, also with improved stability. However, increasing the number of TA-Fe^{III} layers on the NMC created longer Li^+ ion diffusion pathlengths and increased Li^+ ion electrostatic interactions with the negatively charged TA ligands. As a result, the energy barrier that the Li^+ ions have to overcome for the (de)intercalation reaction on the NMC was increased reducing electrochemical performance. It is anticipated that this work with be a precursor to understanding how to enhance battery performance by

optimizing the competitive behavior of enhanced ability of Li^+ ions to reach the NMC and electrostatic interference of metal-phenolic network coated cathode active materials through suitable physicochemical properties of various ligands and metal ions.

Supporting information

Supporting information is available from the Wiley Online Library or from the authors.

Acknowledgements

This work was financially supported by the Electrochemical Testing Project of the Future Battery Industries Cooperative Research Centre (FBICRC). The authors acknowledge Graduate Research Scholarship, University of Melbourne. This work was performed in part at the Materials Characterization and Fabrication Platform (MCFP) at the University of Melbourne. The authors acknowledge the facilities and the scientific and technical assistance of Billy Murdoch and the RMIT University's Microscopy & Microanalysis Facility, a linked laboratory of Microscopy Australia. PCS acknowledges support from RMIT University though the RMIT Vice-Chancellor's Fellowship Scheme (2023). This research was undertaken in part using the MEX-1 beamline at the Australian Synchrotron, part of ANSTO.

Conflict of Interest

The authors declare no conflict of interest.

Data Availability Statement

The data that support the findings of the study are available from the corresponding author upon reasonable request.

Keywords

Lithium-ion batteries, NMC, surface coating, metal phenolic networks, overpotential, lithium-ion accessibility

References

[1] J. M. Tarascon, M. Armand, *Nature* **2001**, 414, 359.
[2] Y. Xia, J. Zheng, C. Wang, M. Gu, *Nano Energy* **2018**, 49, 434.
[3] P. He, H. Yu, H. Zhou, *J. Mater. Chem.* **2012**, 22, 3680.
[4] C. Zhu, R. E. Usiskin, Y. Yu, J. Maier, *Science* **2017**, 358, 1400.
[5] C. W. Park, J. H. Lee, J. K. Seo, W. Y. Jo, D. Whang, S. M. Hwang, Y. J. Kim, *Nat. Commun.* **2021**, 12, 2145.
[6] D. Park, P. C. Sherrell, F. Xie, A. V. Ellis, *J. Mater. Chem. A* **2024**, 12, 4884.

[7] H. Gao, J. Cai, G.-L. Xu, L. Li, Y. Ren, X. Meng, K. Amine, Z. Chen, *Chem. Mater.* **2019**, 31, 2723.
[8] L. Zou, W. Zhao, Z. Liu, H. Jia, J. Zheng, G. Wang, Y. Yang, J.-G. Zhang, C. Wang, *ACS Energy Lett.* **2018**, 3, 2433.
[9] L. Su, K. Jarvis, H. Charalambous, A. Dolocan, A. Manthiram, *Adv. Func. Mater.* **2023**, 33, 2213675.
[10] A. Manthiram, *Nat. Commun.* **2020**, 11, 1550.
[11] J. A. Gilbert, I. A. Shkrob, D. P. Abraham, *J. Electrochem. Soc.* **2017**, 164, A389.
[12] H. Liu, M. Wolfman, K. Karki, Y.-S. Yu, E. A. Stach, J. Cabana, K. W. Chapman, P. J. Chupas, *Nano Lett.* **2017**, 17, 3452.
[13] X. Zhang, Z. Ju, Y. Zhu, K. J. Takeuchi, E. S. Takeuchi, A. C. Marschilok, G. Yu, *Adv. Energy Mater.* **2020**, 11, 2000808.
[14] S. Xu, R. M. Jacobs, H. M. Nguyen, S. Hao, M. Mahanthappa, C. Wolverton, D. Morgan, *J. Mater. Chem. A* **2015**, 3, 17248.
[15] A. M. Wise, C. Ban, J. N. Weker, S. Misra, A. S. Cavanagh, Z. Wu, Z. Li, M. S. Whittingham, K. Xu, S. M. George, *Chem. Mater.* **2015**, 27, 6146.
[16] J. Huang, X. Fang, Y. Wu, L. Zhou, Y. Wang, Y. Jin, W. Dang, L. Wu, Z. Rong, X. Chen, *J. Electroanal. Chem.* **2018**, 823, 359.
[17] L. Liang, G. Hu, F. Jiang, Y. Cao, *J. Alloys Compd.* **2016**, 657, 570.
[18] K. R. Prakasha, M. Sathish, P. Bera, A. S. Prakash, *ACS Omega* **2017**, 2, 2308.
[19] C.-H. Jo, D.-H. Cho, H.-J. Noh, H. Yashiro, Y.-K. Sun, S. T. Myung, *Nano Res.* **2015**, 8, 1464.
[20] C. Yang, X. Zhang, M. Huang, J. Huang, Z. Fang, *ACS Appl. Mater. Interfaces* **2017**, 9, 12408.
[21] F. Yao, F. Gunes, H. Q. Ta, S. M. Lee, S. J. Chae, K. Y. Sheem, C. S. Cojocaru, S. S. Xie, Y. H. Lee, *J. Am. Chem. Soc.* **2012**, 134, 8646.
[22] X. Zhu, T. U. Schulli, X. Yang, T. Lin, Y. Hu, N. Cheng, H. Fujii, K. Ozawa, B. Cowie, Q. Gu, S. Zhou, Z. Cheng, Y. Du, L. Wang, *Nat. Commun.* **2022**, 13, 1565.
[23] R. Dang, M. Chen, Y. Lee, Y. Cheng, L. Xue, Z. Hu, X. Xiao, X. Huang, *Electrochim. Acta* **2017**, 247, 443.
[24] H. Ejima, J. J. Richardson, K. Liang, J. P. Best, M. P. van Koeverden, G. K. Such, J. Cui, F. Caruso, *Science* **2013**, 341, 154.
[25] M. A. Rahim, K. Kempe, M. Müllner, H. Ejima, Y. Ju, M. P. Van Koeverden, T. Suma, J. A. Braunger, M. G. Leeming, B. F. Abrahams, *Chem. Mater.* **2015**, 27, 5825.
[26] M. A. Rahim, M. Björnmalm, N. Bertleff-Zieschang, Y. Ju, S. Mettu, M. G. Leeming, F. Caruso, *ACS Appl. Mater. Interfaces* **2017**, 10, 7632.
[27] J. Guo, Y. Ping, H. Ejima, K. Alt, M. Meissner, J. J. Richardson, Y. Yan, K. Peter, D. Von Elverfeldt, C. E. Hagemeyer, *Angew. Chem. Int. Ed.* **2014**, 53, 5546.
[28] J. Chen, S. Pan, J. Zhou, Q.-Z. Zhong, Y. Qu, J. J. Richardson, F. Caruso, *Chem. Mater.* **2020**, 32, 6975.
[29] X. Su, Y. Luo, Z. Tian, Z. Yuan, Y. Han, R. Dong, L. Xu, Y. Feng, X. Liu, J. Huang, *Mater. Horiz.* **2020**, 7, 2651.
[30] C.-J. Kim, F. Ercole, J. Chen, S. Pan, Y. Ju, J. F. Quinn, F. Caruso, *J. Am. Chem. Soc.* **2021**, 144, 503.
[31] J. Zhou, Z. Lin, Y. Ju, M. A. Rahim, J. J. Richardson, F. Caruso, *Acc. Chem. Res.* **2020**, 53, 1269.
[32] J. Saiz-Poseu, J. Mancebo-Aracil, F. Nador, F. Busqué, D. Ruiz-Molina, *Angew. Chem. Int. Ed.* **2019**, 58, 696.
[33] T. Wang, Z. Lin, O. Mazaheri, J. Chen, W. Xu, S. Pan, C.-J. Kim, J. Zhou, J. J. Richardson, F. Caruso, *Angew. Chem. Int. Ed.* **2024**, e202410043.

[34] O. Mazaheri, M. S. Alivand, A. Zavabeti, S. Spoljaric, S. Pan, D. Chen, F. Caruso, H. C. Suter, K. A. Mumford, *Adv. Func. Mater.* **2022**, 32, 2111942.
[35] X. Chen, K. Li, Z. Yuan, Y. Zhou, J. Xu, L. An, J. Hu, Y. Liu, *ACS Appl. Electron. Mater.* **2022**, 4, 6149.
[36] J. Y. Oh, Y. Jung, Y. S. Cho, J. Choi, J. H. Youk, N. Fechler, S. J. Yang, C. R. Park, *ChemSusChem* **2017**, 10, 1675.
[37] L. Pan, H. Wang, C. Wu, C. Liao, L. Li, *ACS Appl. Mater. Interfaces* **2015**, 7, 16003.
[38] W. Xu, Z. Lin, S. Pan, J. Chen, T. Wang, C. Cortez-Jugo, F. Caruso, *Angew. Chem. Int. Ed.* **2023**, 62, e202312925.
[39] M. A. Rahim, H. Ejima, K. L. Cho, K. Kempe, M. Müllner, J. P. Best, F. Caruso, *Chem. Mater.* **2014**, 26, 1645.
[40] H. Ejima, J. J. Richardson, F. Caruso, *Nano Today* **2017**, 12, 136.
[41] Z.-D. Huang, X.-M. Liu, S.-W. Oh, B. Zhang, P.-C. Ma, J.-K. Kim, *J. Mater. Chem.* **2011**, 21, 10777.
[42] F. Wang, S. Xiao, Z. Chang, Y. Yang, Y. Wu, *Chem. Commun.* **2013**, 49, 9209.
[43] M. Kim, J. Zhu, L. Li, C. Wang, G. Chen, *ACS Appl. Energy Mater.* **2020**, 3, 12238.
[44] D. Ren, E. Padgett, Y. Yang, L. Shen, Y. Shen, B. D. A. Levin, Y. Yu, F. J. DiSalvo, D. A. Muller, H. D. Abruna, *ACS Appl. Mater. Interfaces* **2019**, 11, 41178.
[45] M. H. Tahmasebi, M. N. Obrovac, *J. Electrochem. Soc.* **2023**, 170, 080519
[46] M. Balasubramanian, X. Sun, X.Q. Yang, J. McBreen, *J. Power Sources* **2001**, 92, 1.
[47] R. M. Cinco, K. L. McFarlane Holman, J. H. Robblee, J. Yano, S. A. Pizarro, E. Bellacchio, K. Sauer, V. K. Yachandra, *Biochem.* **2002**, 41, 12928.
[48] K. R. Tallman, G. P. Wheeler, C. J. Kern, E. Stavitski, X. Tong, K. J. Takeuchi, A. C. Marschilok, D. C. Bock, E. S. Takeuchi, *J. Phys. Chem. C* **2020**, 125, 58.
[49] C. Maerten, L. Lopez, P. Lupattelli, G. Rydzek, S. Pronkin, P. Schaaf, L. Jierry, F. Boulmedais, *Chem. Mater.* **2017**, 29, 9668.
[50] A. Noori, M. F. El-Kady, M. S. Rahmanifar, R. B. Kaner, M. F. Mousavi, *Chem. Soc. Rev.* **2019**, 48, 1272.
[51] Y. Shao, M. F. El-Kady, J. Sun, Y. Li, Q. Zhang, M. Zhu, H. Wang, B. Dunn, R. B. Kaner, *Chem. Rev.* **2018**, 118, 9233.
[52] H. Lindström, S. Södergren, A. Solbrand, H. Rensmo, J. Hjelm, A. Hagfeldt, S.-E. Lindquist, *J. Phys. Chem. B* **1997**, 101, 7717.
[53] V. Augustyn, J. Come, M. A. Lowe, J. W. Kim, P.-L. Taberna, S. H. Tolbert, H. D. Abruña, P. Simon, B. Dunn, *Nat. Mater.* **2013**, 12, 518.
[54] J. Wang, J. Polleux, J. Lim, B. Dunn, *J. Phys. Chem. C* **2007**, 111, 14925.
[55] J. Kim, S. Park, S. Hwang, W.-S. Yoon, *J. Electrochem. Sci. Technol.* **2022**, 13, 19.
[56] P.-C. Tsai, B. Wen, M. Wolfman, M.-J. Choe, M. S. Pan, L. Su, K. Thornton, J. Cabana, Y.-M. Chiang, *Energy Environ. Sci.* **2018**, 11, 860.
[57] R. Zhang, C. Wang, P. Zou, R. Lin, L. Ma, L. Yin, T. Li, W. Xu, H. Jia, Q. Li, S. Sainio, K. Kisslinger, S. E. Trask, S. N. Ehrlich, Y. Yang, A. M. Kiss, M. Ge, B. J. Polzin, S. J. Lee, W. Xu, Y. Ren, H. L. Xin, *Nature* **2022**, 610, 67.
[58] C. D. Quilty, D. C. Bock, S. Yan, K. J. Takeuchi, E. S. Takeuchi, A. C. Marschilok, *J. Phys. Chem. C* **2020**, 124, 8119.
[59] D. del Olmo, M. Pavelka, J. Kosek, *J. Non-Equil. Thermody.* **2021**, 46, 91.
[60] W. Li, L. M. Housel, G. P. Wheeler, D. C. Bock, K. J. Takeuchi, E. S. Takeuchi, A. C. Marschilok, *ACS Appl. Energy Mater.* **2021**, 4, 12067.
[61] S. Wang, J. Zhang, O. Gharbi, V. Vivier, M. Gao, M. E. Orazem, *Nat. Rev. Methods Primers* **2021**, 1, 41.
[62] D. Medvedev, *Electrochim. Acta* **2020**, 360, 137034.

[63] A. Maradesa, B. Py, J. Huang, Y. Lu, P. Iurilli, A. Mrozinski, H. M. Law, Y. Wang, Z. Wang, J. Li, *Joule* **2024**, 8, 1958.
[64] F. Weber, E. Sagstuen, Q.-Z. Zhong, T. Zheng, H. Tiainen, *ACS Appl. Mater. Interfaces* **2020**, 12, 52457.
[65] Q. Wu, T. He, Y. Zhang, J. Zhang, Z. Wang, Y. Liu, L. Zhao, Y. Wu, F. Ran, *J. Mater. Chem. A* **2021**, 9, 24094.
[66] Y. Lu, C.-Z. Zhao, J.-Q. Huang, Q. Zhang, *Joule* **2022**, 6, 1172.
[67] X. Liu, G.-L. Xu, V. S. C. Kolluru, C. Zhao, Q. Li, X. Zhou, Y. Liu, L. Yin, Z. Zhuo, A. Daali, J.-J. Fan, W. Liu, Y. Ren, W. Xu, J. Deng, I. Hwang, D. Ren, X. Feng, C. Sun, L. Huang, T. Zhou, M. Du, Z. Chen, S.-G. Sun, M. K. Y. Chan, W. Yang, M. Ouyang, K. Amine, *Nat. Energy* **2022**, 7, 808.
[68] P. Liu, X.-Y. Kong, L. Jiang, L. Wen, *Chem. Soc. Rev.* **2024**, 53, 2972.
[69] E. Adhitama, F. Demelash, T. Brake, A. Arifiadi, M. Vahnstiege, A. Javed, M. Winter, S. Wiemers-Meyer, T. Placke, *Adv. Energy Mater.* **2024**, 14, 2303468.
[70] R. Zhang, Y. Zheng, Z. Yao, P. Vanaphuti, X. Ma, S. Bong, M. Chen, Y. Liu, F. Cheng, Z. Yang, *ACS Sustainable Chem. Eng.* **2020**, 8, 9875.
[71] J. Zhou, D. Danilov, P. H. Notten, *Chem. Eur. J.* **2006**, 12, 7125.
[72] A. Jana, S. I. Woo, K. S. N. Vikrant, R. E. García, *Energy Environ. Sci.* **2019**, 12, 3595.
[73] L. Yu, S. Chen, H. Lee, L. Zhang, M. H. Engelhard, Q. Li, S. Jiao, J. Liu, W. Xu, J.-G. Zhang, *ACS Energy Lett.* **2018**, 3, 2059.
[74] R. Tian, S. H. Park, P. J. King, G. Cunningham, J. Coelho, V. Nicolosi, J. N. Coleman, *Nat. Commun.* **2019**, 10, 1933.
[75] F. Cheng, X. Zhang, Y. Qiu, J. Zhang, Y. Liu, P. Wei, M. Ou, S. Sun, Y. Xu, Q. Li, *Nano Energy* **2021**, 88, 106301.
[76] J. Li, W. Li, Y. You, A. Manthiram, *Adv. Energy Mater.* **2018**, 8, 1801957.
[77] J. Kasnatscheew, T. Placke, B. Streipert, S. Rothermel, R. Wagner, P. Meister, I. C. Laskovic, M. Winter, *J. Electrochem. Soc.* **2017**, 164, A2479.

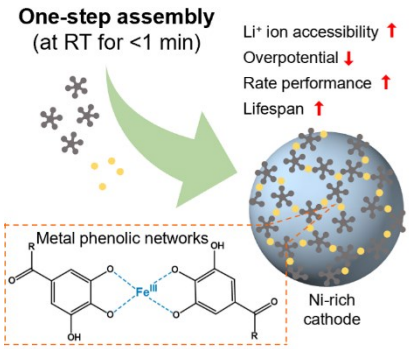

Surface coating strategies have emerged to optimize cathodic LIB performance or to suppress failure mechanisms. However, previously adopted coatings require several hours for synthesis including a high temperature calcination. Metal phenolic networks coating layer synthesised by one-step assembly (at RT for < 1 min) enhances the lithium-ion accessibility of NMC, resulting in reduced overpotential, and improving battery performance and lifespan.